Research Square

Preprints are preliminary reports that have not undergone peer review.
They should not be considered conclusive, used to inform clinical practice,
or referenced by the media as validated information.

Adaptive edge-preserving denoising using a gradient-based delta-map for NDT X-ray imaging

Jaehong Hwang
Korea Research Institute of Standards and Science
Junwoo Kim
junwookim@dongnam.ac.kr
Dongnam Health University

Research Article

Keywords: NDT X-ray imaging, edge-enhancement, noise-reduction, image quality

Posted Date: September 8th, 2026

DOI: https://doi.org/10.21203/rs.3.rs-9893419/v1

License: This work is licensed under a Creative Commons Attribution 4.0 International License. Read Full License

Additional Declarations: No competing interests reported.

Abstract

In medical imaging and industrial non-destructive testing (NDT), preserving structural features while suppressing noise presents a fundamental trade-off. To overcome this limitation, this study proposes an adaptive image processing (AIP) technique utilizing a gradient-based delta-map (δ -map) that generates pixel-wise weights based on the local gradient magnitudes. The proposed method quantifies the structural salience of the input image to generate a δ -map and applies it to a residual-based enhancement process, thereby selectively suppressing noise in homogeneous regions while enhancing sharpness in edge regions. Experimental results on printed circuit board (PCB) X-ray images demonstrated that the proposed method yielded superior visual quality compared to conventional filters with globally fixed parameters (e.g., Gaussian, unsharp masking, bilateral) and commercial algorithms (MUSICA). Consistent performance improvements were confirmed through quantitative metrics (SSIM, PSNR, LPIPS) and no-reference image quality assessments (BRISQUE, NIQE). Furthermore, analysis of the modulation transfer function (MTF), noise power spectrum (NPS), and noise-equivalent quanta (NEQ) verified that the proposed method optimizes signal transfer characteristics across a wide frequency range while minimizing spatial resolution degradation. Unlike deep learning approaches, this method offers high computational efficiency and algorithmic interpretability, providing a practical solution immediately applicable to real-time X-ray inspection systems.

1. Introduction

The primary objective in medical and industrial non-destructive testing (NDT) imaging is the accurate and reliable identification of structural features, such as lesions or defects [1–3]. To achieve this, appropriate modulation of the spatial resolution and noise characteristics is essential. However, these two factors exhibit a fundamental physical trade-off [4]. Enhancing high-frequency components sharpens edges and ridge structures but simultaneously amplifies systematic noise, degrading the reliability of diagnosis or defect detection [5]. Conversely, applying low-pass filters for noise suppression impairs the detectability of micro-structures and overall image interpretability [6]. This constraint is consistently mathematically defined in classical radiographic system theory evaluated via the modulation transfer function (MTF), noise power spectrum (NPS), and detective quantum efficiency (DQE), resolution and noise act as coupled axes of system performance that cannot be independently improved [7–9]. In general, conventional filtering techniques ranging from basic Gaussian and unsharp masking (UM) to edge-preserving models like bilateral [10], guided [11], non-local means [12], and total variation (TV) [13] have been widely utilized for image enhancement. Although these methods benefit from simple implementation, they predominantly rely on globally fixed hyperparameters. This constraint makes it difficult to consistently achieve optimal performance in practical imaging environments where structurally heterogeneous regions coexist. For instance, in printed circuit board (PCB) X-ray imaging containing high-frequency structures (e.g., solder joints or conductor patterns) coexist with uniform low-frequency substrate regions. Applying spatially invariant parameters across such distinct regions inherently fails to achieve optimal image quality. To overcome these limitations, spatially adaptive processing techniques [10], [13], [14] and deep learning-based enhancement methods [15–17] have been proposed. However, deep learning approaches require large-scale training datasets and heavy computational resources. Furthermore, their application to practical industrial inspection equipment is fundamentally restricted by a lack of analytic interpretability and hardware constraints [18]. Therefore, this study proposes a gradient-based $\backslash\mathrm{varvec}\delta$ -map adaptive image processing ($\backslash\mathrm{varvec}\delta$ -AIP) framework that quantifies structural salience at the pixel level and directly incorporates it into the enhancement process. The proposed $\backslash\mathrm{varvec}\delta$ -map is defined not merely as a simple scalar coefficient, but as a structural salience regulator representing the significance of each pixel. Through this spatially variant application, the proposed method mitigates the resolution-noise trade-off by selectively enhancing sharpness in structural features while suppressing noise in homogeneous areas. The performance of the proposed method was evaluated using printed circuit board (PCB) X-ray images via qualitative assessments, as well as quantitative full-reference (PSNR, SSIM, LPIPS) [19–21] and no-reference (BRISQUE, NIQE, PIQE) metrics [22–24]. Furthermore, cascaded systems analysis utilizing the modulation transfer function (MTF), noise power spectrum (NPS), and noise-equivalent quanta (NEQ) was conducted to verify that the proposed method

optimizes signal transfer characteristics across a wide frequency range while minimizing spatial resolution degradation [8], [25].

2. Materials and Methods

2.1. Basic Principles and Algorithm Overview

The proposed $\varvec{\delta}$ -map-based adaptive image processing algorithm extends the residual-based architecture of the traditional unsharp masking (UM). The conventional UM technique amplifies the high-frequency components by extracting the difference between the original image and its low-pass filtered counterpart. However, applying a globally fixed parameter often leads to severe noise amplification or halo artifacts along structural boundaries in heterogeneous images. To overcome this, the proposed method retains the linear combination structure of UM but introduces a spatially variant coefficient, $\delta(i,j)$, computed at each pixel location (i,j). This deterministic design automatically modulates the spatial operation, switching between edge sharpening and noise smoothing based on the local structural characteristics quantified by gradient mapping. The overall flowchart of the proposed framework is illustrated in Fig. 1.

2.2. $\varvec{\delta}$ -map Generation Procedure

In this framework, all boldface variables denote 2D spatial matrices representing images or parameter maps, and all algebraic operations are performed element-wise unless otherwise specified. The proposed $\varvec{\delta}$ -map is constructed through a systematic multi-stage procedure designed to adaptively capture the local structural salience of the image. The detailed methodology is as follows.

2.2.1. Gradient Magnitude Calculation

First, an isotropic Gaussian filter (G) is applied to the original image ($\mathbf{I}_{\text{org}}$) to mitigate high-frequency noise prior to differentiation [26].

$$\mathbf{I}_{\text{LPF}} = G * \mathbf{I}_{\text{org}} \qquad (1)$$

where $\mathbf{I}_{\text{LPF}}$ is the Gaussian filtered image. The standard deviation of the Gaussian kernel is a tunable parameter dependent on the noise level of the input image.

Subsequently, Sobel filters (horizontal and vertical derivative kernels, K_x and K_y) are applied to compute the gradient magnitude matrix $\mathbf{M}$ [27–29], which serves as a key metric for characterizing localized structural boundaries.

$$\mathbf{M} = \sqrt{(K_x * \mathbf{I}_{\text{LPF}})^2 + (K_y * \mathbf{I}_{\text{LPF}})^2} \qquad (2)$$

2.2.2. Gradient Magnitude Normalization

Because the absolute gradient magnitude exhibits severe scale variations depending on the global image contrast, a percentile-based normalization is performed. Let τ_{Low} and τ_{High} denote the threshold scalar values corresponding to the lower 5% and upper 95% of the percentiles of the entire distribution of $\mathbf{M}$. To ensure robustness against impulse noise and outlier gradients, a bounded clipping operator is explicitly integrated [30].

$$\mathbf{M}_{\text{Nor}} = \max\left[0, \min\left(1, \frac{\mathbf{M}-\tau_{\text{Low}}}{\tau_{\text{High}}-\tau_{\text{Low}}}\right)\right] \qquad (3)$$

where $\mathbf{M}_{\text{Nor}}$ is the normalized gradient magnitude matrix.

2.2.3. $\varvec{\delta}$ -map Construction

A mapping function is applied to convert the normalized gradient into a preliminary weight matrix $\mathrm{varvec}\delta_{\mathrm{pre}}$, ensuring smooth control over the transient region between the structural features and homogeneous areas. While various nonlinear transformations like sigmoid, gamma, or hyperbolic tangent are applicable, a linear function ($\mathrm{varvec}\delta_{\mathrm{pre}} = \mathbf{M}_{\mathrm{Nor}}$) was adopted as the baseline in this study to minimize model complexity and isolate the intrinsic effect of the δ-map. A detailed analysis regarding the effects of various nonlinear transformations on image features is provided in the discussion section.

$$\mathrm{varvec}\delta = w_{\min} + \mathrm{varvec}\delta_{\mathrm{pre}} \cdot (w_{\max} - w_{\min}) \qquad (4)$$

This scaling structure is based on the adaptive unsharp masking (UM) method [31]. To simultaneously achieve noise suppression in the background regions and sharpness enhancement in the edge regions, the scaling parameters in Eq. (4) are empirically set to $w_{\min}$ = -0.5 and $w_{\max}$ = 1.0. Consequently, this configuration induces a low-pass filtering effect where $\mathrm{varvec}\delta$ < 0 and amplifies high-frequency components where $\mathrm{varvec}\delta$ > 0. The resulting $\mathrm{varvec}\delta$-map is visually represented in Fig. 2.

As shown in Fig. 2, the PCB X-ray image is categorized into noise-sensitive and edge-critical regions. Green-coded areas represent low-gradient, homogeneous regions where noise reduction is prioritized. Conversely, red-coded areas correspond to structural components including solder ball joints or conductor patterns, which are targeted for edge preservation and enhancement. This adaptive approach ensures that parameters are dynamically tuned for each pixel to balance noise suppression with structural fidelity.

2.2.4. Adaptive Image Reconstruction

First, the high-frequency residual matrix ($\mathbf{I}_{\mathrm{HPF}}$) is extracted by subtracting the low-pass filtered image ($\mathbf{I}_{\mathrm{LPF}}$) from the original image ($\mathbf{I}_{\mathrm{org}}$) [32].

$$\mathbf{I}_{\mathrm{HPF}} = \mathbf{I}_{\mathrm{org}} - \mathbf{I}_{\mathrm{LPF}} \qquad (5)$$

where $\mathbf{I}_{\mathrm{LPF}}$ is the low-pass filtered image by Gaussian kernel.

To selectively target specific residual frequency bands for enhancement, the standard deviation of the Gaussian kernel for $\mathbf{I}_{\mathrm{LPF}}$ in Eq. (5) can be adjusted. The extracted matrix $\mathbf{I}_{\mathrm{HPF}}$ effectively isolates high-frequency features such as edges, ridges, and fine textures. The final adaptively enhanced image, $\mathbf{I}_{\mathrm{AIP}}$, is reconstructed via an element-wise linear combination in Eq. (6).

$$\mathbf{I}_{\mathrm{AIP}} = \mathbf{I}_{\mathrm{org}} + \mathrm{varvec}\delta \circ \mathbf{I}_{\mathrm{HPF}} \qquad (6)$$

where $\mathbf{I}_{\mathrm{AIP}}$ is the proposed delta-map based adaptive image processing result and $\circ$ denotes the Hadamard (element-wise) product.

According to the scaling boundaries established in Eq. (4), if $\mathrm{varvec}\delta$ > 0, high-frequency components are amplified to enhance structural sharpness, whereas for $\mathrm{varvec}\delta$ < 0, high-frequency components are suppressed to reduce noise in uniform regions. This pixel-wise adaptive mechanism effectively overcomes the limitations of global parameter-based filters, which struggle with structural nonlinearity. Consequently, the proposed approach is particularly well-suited for NDT imaging of PCBs, characterized by significant structural heterogeneity.

2.3. Comparison Algorithms

To verify the performance of the proposed framework, a comparative analysis was conducted against five representative algorithms widely utilized in the image enhancement domain. The selected comparison algorithms and their theoretical characteristics are as follows.

Gaussian filter [29]: The most conventional low-pass smoothing technique, effectively mitigating high-frequency noise using an isotropic kernel. However, by applying uniform smoothing without distinguishing between noise and structural features, it

inherently induces structural blurring.

Unsharp masking (UM) [31]: A classical sharpening method that amplifies high-frequency components via a constant scalar coefficient. While advantageous for its computational efficiency, its reliance on a fixed global coefficient frequently causes halo artifacts along structural boundaries and noise amplification in background regions.

Bilateral filter [10]: A prominent edge-preserving smoothing operator that simultaneously considers spatial Euclidean distance and pixel intensity differences. Nevertheless, optimizing its spatially invariant parameters for images with heterogeneous contrast levels poses a significant challenge, accompanied by a substantial computational burden.

Guided filter [11]: An advanced edge-preserving algorithm that constructs a local linear regression model based on a guidance image, achieving rapid processing speed and low gradient-reversal artifacts. Although more stable than the bilateral filter, it remains highly sensitive to a globally set regularization parameter, limiting its localized adaptability across diverse sub-regions.

Multiscale image contrast amplification (MUSICA) [33]: A commercial medical image processing framework widely adopted in radiographic imaging for enhancing contrast across multiscale Laplacian pyramids. While it significantly improves overall visual quality, its layer-specific weights are applied globally across the entire spatial domain, limiting optimal structural preservation in NDT images characterized by severe geometric heterogeneity.

In summary, although the aforementioned algorithms exhibit distinct strengths in either structural preservation or noise suppression, they share a fundamental limitation due to their reliance on spatially invariant parameters. This constraint precludes them from consistently achieving optimal performance in real-world scenarios where high-frequency structural details and low-frequency uniform backgrounds coexist. In contrast, the proposed framework natively resolves this limitation by quantifying structural salience at the pixel level. The characteristics of these algorithms are summarized in Table 1.

Table 1

Summary of the comparison algorithms used in this study with their representative formulations. In all formulations, $\mathbf{I}_{\text{org}}$ denotes the original input image matrix.

Algorithm	Principle	Representative Formulation	Key Parameter & Scope	Primary Limitation in NDT
Gaussian Filter	Isotropic low-pass smoothing	$\mathbf{I}_{\text{Gaussian}} = G_\sigma * \mathbf{I}_{\text{org}}$ where G is the Gaussian kernel, and σ is the standard deviation.	σ (Global)	Edge blurring
Unsharp Masking (UM)	Residual-based sharpening	$\mathbf{I}_{\text{UM}} = \mathbf{I}_{\text{org}} + k \cdot (\mathbf{I}_{\text{org}} - \mathbf{I}_{\text{Gaussian}})$ where k is the constant amplification factor.	k (Global)	Halo artifacts & noise amplification
Bilateral Filtering	Edge-preserving smoothing	$\mathbf{I}_{\text{BF}}(p) = \frac{1}{W_p}\sum_q G_{\sigma_s}(\|p-q\|)\, G_{\sigma_r}\left(\left\|\mathbf{I}_{\text{org}}(p) - \mathbf{I}_{\text{org}}(q)\right\|\right)\mathbf{I}_{\text{org}}(q)$ where p, q are spatial pixel indices, G_{σ_s} and G_{σ_r} are spatial and range Gaussian kernels, and W_p is the normalization factor.	σ_s, σ_r (Global)	Computational cost, parameter sensitivity
Guided Filter	Local linear model	$\mathbf{I}_{\text{Guided}}(i) = a_k \mathbf{I}_{\text{org}}(i) + b_k, (\forall i \in \omega_k)$ $a_k = \frac{\sigma_k^2}{\sigma_k^2+\epsilon}$, $b_k = \mu_k - a_k\mu_k$ where i is the pixel index, and μ_k, σ_k^2 are the local mean and variance within the local window ω_k of radius r, and ϵ is the regularization parameter.	r, ϵ (Global)	Limited localized adaptability
MUSICA	Multiscale contrast amplification	$\mathbf{I}_{\text{MUSICA}} = \sum_{s=1}^{S} w_s \mathbf{B}_s$ where S is the total number of scales, $\mathbf{B}_s$ is the s-th bandpass layer, and w_s is the multiscale contrast amplification weight.	w_s (Global)	Suboptimal structural preservation

Algorithm	Principle	Representative Formulation	Key Parameter & Scope	Primary Limitation in NDT
Ours* ($\varvec{\delta}$-AIP)	Pixel-wise adaptive modulation	$\mathbf{I}_{\mathrm{AIP}} = \mathbf{I}_{\mathrm{org}} + \varvec{\delta} \circ \mathbf{I}_{\mathrm{HPF}}$ where $\varvec{\delta}$ is the proposed pixel-wise adaptive control matrix, $\mathbf{I}_{\mathrm{HPF}}$ is the high-frequency residual matrix, and $\circ$ is the Hadamard product.	$\varvec{\delta}$ (Pixel-wise)	-

2.4 Experimental Setup and Data Acquisition

To verify the proposed algorithm, X-ray images of a printed circuit board (PCB) specimen were acquired using a laboratory-scale radiographic imaging system [34]. These images inherently contain a mixture of high-frequency components (solder balls and wire traces), and low-frequency components (homogeneous regions). The system configuration is illustrated in Fig. 3(a). The measurement system consisted of a tungsten-target X-ray tube (E7239X, Toshiba Co. Ltd.) and an image detector based on a coupled structure of a phosphor screen and a photodiode array. Specifically, a RadEye1™ detector (Teledyne DALSA, Waterloo, ON, Canada) was employed, featuring a 512 × 1024 array with a pixel pitch of 0.048 mm. A Gd_2O_2S:Tb scintillator screen with a mass thickness of 33.91 mg/cm² was applied. The X-ray exposure conditions for image acquisition were set to 90 kVp and 2.5 mAs. Subsequently, all acquired images underwent calibration procedures, including pixel-wise gain-offset corrections [35], along with defective pixel interpolation [36]. Furthermore, Gaussian noise (σ_n = 2.0) was intentionally added to the acquired images to quantitatively evaluate the edge-preserving and noise-reduction performance of the proposed method. The clean reference image (ground truth) and the image with added Gaussian noise are shown in Fig. 3(b) and Fig. 3(c), respectively.

2.5. Quantitative Image Quality Metrics

Image quality assessment is a critical procedure to quantitatively verify how effectively the proposed algorithm balances structural preservation and noise suppression. Particularly in NDT imaging, factors such as edge fidelity, noise levels, and the presence of perceptual artifacts serve as direct criteria for defect detection. In this study, full-reference (FR-IQA) and no-reference (NR-IQA) metrics were employed to comprehensively evaluate both structural accuracy and perceptual quality. Specifically, FR-IQA metrics were applied to synthetic datasets with ground-truth references, whereas NR-IQA metrics were utilized for real-world NDT images lacking reference counterparts. This multi-layered validation framework is essential for establishing the practical efficacy of the proposed technique. The evaluated metrics and their mathematical principles are summarized in Table 2.

Table 2
Summary of FR-IQA and NR-IQA metrics used in this study. The detailed mathematical definitions follow their original references. In this work, representative equations are presented to emphasize the interpretative role of each metric.

Category	Metric	Evaluation Aspect	Representative Equation
FR-IQA	SSIM	Structural similarity & fidelity	$\mathrm{SSIM}(\mathbf{x},\mathbf{y}) = \left(\frac{2\mu_x\mu_y + C_1}{\mu_x^2+\mu_y^2+C_1}\right)\left(\frac{2\sigma_{xy}+C_2}{\sigma_x^2+\sigma_y^2+C_2}\right)$ where μ and σ^2 are the local mean and variance, σ_{xy} is the local covariance, and C_1, C_2 are stabilization constants.
	PSNR	Pixel-level signal fidelity	$\mathrm{PSNR} = 10 \cdot \log_{10}\left(\frac{\mathrm{MAX_I}^2}{\mathrm{MSE}}\right)$ where $\mathrm{MAX_I}$ is the maximum possible pixel intensity, and MSE is the mean squared error between $\mathbf{x}$ and $\mathbf{y}$.
	LPIPS	Deep perceptual similarity	$\mathrm{LPIPS}(\mathbf{x},\mathbf{y}) = \sum_l \frac{1}{H_l W_l}\sum_{h,w}\left\|\mathbf{w}_l \circ \left(\hat{\mathrm{f}}_x^l(h,w) - \hat{\mathrm{f}}_y^l(h,w)\right)\right\|_2^2$ where H_l, W_l are spatial dimensions at layer l, $\mathbf{w}_l$ is the channel weight vector, and $\hat{\mathrm{f}}_x^l$ and $\hat{\mathrm{f}}_y^l$ are the channel-normalized feature maps of $\mathbf{x}$ and $\mathbf{y}$, and $\circ$ denotes the Hadamard product.
NR-IQA	BRISQUE	Natural scene statistics (NSS) quality	$\mathrm{BRISQUE} = f_{\mathrm{SVR}}\left(\mathbf{f}_{\mathrm{MSCN}}\right)$ where $\mathbf{f}_{\mathrm{MSCN}}$ represents the features extracted from the mean subtracted contrast normalized (MSCN) coefficients, and f_{SVR} is the pre-trained support vector regression model.
	NIQE	Unsupervised statistical naturalness	$\mathrm{NIQE} = \sqrt{(\varvec{\mu}_1 - \varvec{\mu}_2)^T\left(\frac{\varvec{\Sigma}_1+\varvec{\Sigma}_2}{2}\right)^{-1}(\varvec{\mu}_1 - \varvec{\mu}_2)}$ where $\varvec{\mu}$ and $\varvec{\Sigma}$ are the mean vectors and covariance matrices of the multivariate Gaussian models for the pristine and distorted images, respectively.
	PIQE	Block-wise perceptual distortion	$\mathrm{PIQE} = \frac{1}{N_A}\sum_{k=1}^{N_A} D_k$

Category	Metric	Evaluation Aspect	Representative Equation
			where N_A is the total number of spatially active blocks, and D_k is the computed distortion score for the k-th active block.

2.5.1. Full-Reference Image Quality Assessment Metrics

For experimental conditions where a reference ground-truth image is available, the following full-reference metrics were utilized.

Structural similarity index (SSIM) [19]: A visual quality metric that evaluates the similarity between two images by decomposing the information into luminance, contrast, and structural components. Unlike simple pixel-difference metrics, it inherently reflects the structural sensitivity of the human visual system, and was thus employed to evaluate how effectively the proposed technique preserves edge and ridge structures.

Peak signal-to-noise ratio (PSNR) [20]: A traditional image quality metric based on the mean squared error (MSE), useful for evaluating overall noise suppression levels and signal preservation. In this work, it was used to quantitatively analyze the extent to which the proposed framework reduces high-frequency noise in homogeneous regions.

Learned perceptual image patch similarity (LPIPS) [21]: A deep learning-based metric that measures the perceptual distance between two images within the feature space of a pre-trained convolutional neural network (CNN). Exhibiting high sensitivity to visual artifacts such as ringing and localized contrast distortions, it was utilized to verify whether the proposed method enhances structural preservation without compromising perceptual naturalness.

2.5.2. No-Reference Image Quality Assessment Metrics

Because ground truth images are typically unavailable in practical medical and industrial inspection environments, representative no-reference image quality assessment metrics were incorporated.

Blind/referenceless image spatial quality evaluator **(**BRISQUE**)** [22]: A quality assessment tool based on natural scene statistics (NSS) that effectively detects deviations from statistical regularity caused by increased noise or artificial patterns. In this study, it was applied to evaluate the overall statistical stability of the proposed method.

Natural image quality evaluator (NIQE) [23]: A completely unsupervised metric that relies solely on a statistical model derived from high-quality natural images, without requiring subjective quality labels. Since it is highly sensitive to overall unnaturalness, it was used to verify that the proposed technique does not induce excessive sharpening or artificial artifacts.

Perception-based image quality evaluator (PIQE) [24]: A spatial domain metric that evaluates localized distortions, such as ringing and overshoot, through block-wise local analysis. It was utilized to further confirm that the proposed algorithm effectively suppresses artifacts near complex structural boundaries.

2.6. Spatial Frequency Analysis

To quantitatively evaluate the effect of the image processing algorithms on the spatial frequency characteristics of the images, the modulation transfer function (MTF), noise power spectrum (NPS), and noise-equivalent quanta (NEQ) were calculated. These three metrics are fundamental standards widely used in digital radiography to comprehensively assess the resolution, noise characteristics, and overall detection performance of an imaging system [8], [25].

The MTF represents the fidelity with which a system transfers contrast as a function of spatial frequency, serving as a standard metric for spatial resolution assessment across various imaging modalities, including digital radiography, computed tomography (CT), and industrial high-energy X-ray systems [37–39]. Theoretically, the MTF is the frequency-

domain representation of the system's impulse response, ideally calculated using the line-spread function (LSF) acquired from an ideal slit or pinhole. However, fabricating and measuring an ideal slit phantom is physically challenging. Therefore, in accordance with the IEC 62220-1-3 [40] and the methods previously proposed [41], [42], this study calculated the MTF based on the edge-spread function (ESF) using an edge-knife phantom in Eq. (7).

$$\mathrm{MTF}\left(f\right)=\left|\mathcal{F}\left\{\mathrm{LSF}\left(x\right)\right\}\right|=\left|\mathcal{F}\left\{\frac{d}{dx}\mathrm{ESF}\left(x\right)\right\}\right| \qquad (7)$$

where $\mathcal{F}$ denotes the Fourier transform operator.

The ESF was obtained by profiling the edge image along the x or y-axis. The LSF was subsequently derived via differentiation of the ESF, followed by a Fourier transform to compute the presampled MTF. Because the MTF characteristically decreases as spatial frequency increases, it accurately evaluates how well an image processing filter preserves frequency components.

Although image noise can be quantified simply by pixel intensity variance (σ^2), a single variance value obtained in the spatial domain cannot describe the filtering effects and frequency-dependent noise distribution of the system. Thus, employing the NPS, which directly analyzes the spatial frequency components of noise, is considered a more accurate approach [43]. The NPS is mathematically defined as follows.

$$\mathrm{NPS}(u,v)=\frac{\Delta\,x\Delta\,y}{N_xN_y}\left\langle\left|\mathcal{F}\left\{\mathbf{I}\left(x,y\right)-\mu\right\}\right|^2\right\rangle \qquad (8)$$

where u and v are the spatial frequency variables, $\mathbf{I}\left(x,y\right)$ is the pixel intensity at spatial coordinates (x,y), $\Delta\,x$ and $\Delta\,y$ represent the pixel pitch, N_x and N_y denote the size of the region of interest (ROI), and μ is the mean signal intensity within the ROI, and $\langle\bullet\rangle$ denotes the ensemble average across multiple ROIs. The NPS is essential for determining whether image noise is disproportionately concentrated at specific spatial frequencies.

To evaluate the intrinsic noise characteristics while excluding the influence of linear and nonlinear image processing applied to the flat-field images, the noise power spectrum was normalized by the corresponding mean image signal, and the normalized noise power spectrum (NNPS) was subsequently compared. The NEQ combines the MTF and NNPS to indicate how effectively an actual imaging system transfers information [8], as defined in Eq. (9).

$$\mathrm{NEQ}\left(f\right)=\frac{\mathrm{MTF}(f)^2}{\mathrm{NNPS}(f)} \qquad (9)$$

where f is the spatial frequency, and $\mathrm{NNPS}\left(f\right)$ is the 1D radially averaged profile derived from the 2D $\mathrm{NPS}(u,\ v)$.

A higher NEQ implies that a greater number of effective quanta are transferred under identical conditions, which consequently leads to a higher signal-to-noise ratio (SNR) and detective quantum efficiency (DQE).

3. Results

3.1. Qualitative Evaluation

As illustrated in Fig. 4 the performance of the proposed δ -AIP was evaluated in two different ROIs on the PCB radiograph to independently analyze structural preservation and noise suppression. First, the line profile extracted from ROI 1 was analyzed to verify the sharpness of structural boundaries. The profile demonstrates a distinct edge enhancement compared to the conventional UM method, as shown in Fig. 4 (b). Additionally, the pixel intensity distribution of the uniform region in ROI 2 confirms the robust noise suppression of the proposed framework. The result shows that the proposed method effectively reduces the intensity variance while preserving the mean signal intensity, as shown in Fig. 4 (c). This pixel-wise adaptive mechanism is visually validated through a broader qualitative comparison in Fig. 5. While conventional global

filters (Figs. 5(b)–5(f)) inherently suffer from a trade-off between edge enhancement and noise amplification, the proposed δ -AIP effectively suppresses background noise while maintaining structural boundaries without inducing image artifacts such as ringing or halos.

3.2. Quantitative Evaluation

To numerically evaluate the overall image quality, a comprehensive comparison was conducted using full-reference metrics (SSIM, PSNR, LPIPS) and no-reference metrics (BRISQUE, NIQE, PIQE) as summarized in Table 3. Regarding the FR-IQA metrics, the guided filter exhibited the highest SSIM (0.9854) and PSNR (36.618 dB). However, the proposed method maintained competitive structural fidelity (SSIM = 0.9751, PSNR = 33.001 dB) and achieved the lowest LPIPS score alongside the guided filter and MUSICA. This indicates that the proposed method preserves deep-feature perceptual similarity without significant structural degradation. For the NR-IQA metrics, which evaluate blind perceptual quality and naturalness, the proposed method demonstrated distinct advantages. It achieved the lowest BRISQUE (23.736) and PIQE (40.747) scores among all compared algorithms. These results quantitatively indicate that the proposed method effectively suppresses localized distortions and preserves natural scene statistics better than conventional global filters. Overall, the quantitative data substantiates that the $\varvec{\delta}$ -AIP framework provides a stable balance between structural preservation and the reduction of perceptual artifacts.

Table 3
Full-reference and no-reference IQA metrics used in this work.

Algorithm	FR-IQA			NR-IQA			Score
	SSIM	PSNR	LPIPS	BRISQUE	NIQE	PIQE	
Gaussian	0.9646	29.545	0.00017	41.909	5.897	66.455	0
UM	0.9727	32.593	0.00008	36.287	11.165	55.325	0
Bilateral	0.9846	33.022	0.00015	43.333	**4.818**	56.669	1
Guided	**0.9854**	**36.618**	**0.00006**	35.128	10.656	51.734	**3**
MUSICA	0.9819	34.433	**0.00006**	40.545	10.374	50.913	1
Ours*	0.9751	33.001	**0.00006**	**23.736**	8.280	**40.747**	**3**

3.4 Frequency-Domain Performance Evaluation

Figure 6 illustrates the spatial frequency characteristics of the proposed $\varvec{\delta}$ -AIP technique compared to conventional methods in terms of MTF, Normalized NPS (NNPS), and NEQ.

As shown in Fig. 6(a), the Gaussian filter exhibits rapid attenuation even in the low-frequency range, with its modulation transfer ratio converging to zero at spatial frequencies above approximately $3\ \mathrm{mm}^{-1}$, failing to transfer fine structural information. While the UM, bilateral, guided, and MUSICA techniques maintain relatively higher MTF values than the Gaussian filter, they decrease sharply in the mid-frequency band (approximately $4-7\ \mathrm{mm}^{-1}$), revealing a clear limitation in the stable preservation of microscopic features. Conversely, the proposed technique consistently outperforms all comparative methods across the mid- to high-frequency bands (up to $10\ \mathrm{mm}^{-1}$). This exceptional resolution preservation is achieved because the $\varvec{\delta}$ -map selectively amplifies the high-frequency residual components ($\mathbf{I}_{\mathrm{HPF}}$) exclusively within structurally prominent regions, thereby minimizing the loss of high-frequency information.

The NNPS results in Fig. 6(b) further highlight the distinct advantages of the proposed framework. Although the Gaussian filter reduces the overall NNPS, this represents a severe resolution-noise trade-off, as confirmed by its MTF response. The bilateral and guided filters exhibit substantial noise reduction performance in the low-frequency region, but their NNPS increases in the mid-to-high frequency bands, indicating a suboptimal balance between structural preservation and noise

suppression. In contrast, the proposed method achieves a consistently lower and more stable NNPS relative to the edge-preserving filters across all frequency bands, while simultaneously maintaining a higher spatial resolution than the Gaussian filter. This provides empirical evidence that the pixel-wise modulation of the $\varvec{\delta}$-map effectively applies targeted smoothing to noise-dominant areas without amplifying high-frequency noise.

The coupled effects of MTF and NNPS are quantitatively synthesized in the NEQ results, as shown in Fig. 6(c). The proposed method not only preserves a higher SNR than the original image in the low-frequency band but also maintains a consistent quantitative advantage over comparative techniques in the mid-frequency range. Crucially, in the high-frequency regime, most conventional methods, with the exception of the bilateral filter, exhibit severe NEQ attenuation indicating a critical loss of information transfer capability. In contrast, the proposed method sustains statistically robust NEQ levels, successfully transferring high-frequency structural components. Consequently, the proposed framework effectively mitigates the inherent trade-off between resolution and noise. This performance is validated through three physics-based evaluation metrics (MTF, NNPS, and NEQ), confirming the structural and statistical effectiveness of the proposed enhancement scheme.

4. Discussion

The proposed framework addresses the fundamental limitations of conventional spatially invariant filtering architectures. Its primary contribution is the spatially adaptive modulation depending on localized structural salience. First, conventional filters apply a single global parameter setting, such as the standard deviation of Gaussian kernel or the amplification factor in unsharp masking, uniformly across the entire image. This rigid approach inevitably leads to a trade-off where a parameter set optimized for one region becomes sub-optimal for another. The proposed $\varvec{\delta}$-map effectively overcomes this global rigidity by enabling spatially adaptive and continuous modulation between structural regions (where the $\varvec{\delta}$ increases) and homogeneous flat regions (where the $\varvec{\delta}$ decreases). Second, unlike data-driven deep learning approaches, the proposed method does not require subjective human labels or extensive training datasets. It operates on clear, deterministic structural principles, eliminating the opacity of deep learning models. This level of interpretability and predictability is essential in medical diagnostics and reliable industrial NDT environments. Third, because the calculation of $\varvec{\delta}$-map is composed of straightforward mathematical operations based on the gradient magnitude, the framework can be easily implemented for real-time processing on hardware accelerators such as GPUs or embedded FPGAs.

The performance variations under different mapping functions are illustrated in Fig. 7. The top row displays the distinct characteristics of the extracted $\varvec{\delta}$-maps when using linear, sigmoid, gamma, and tanh functions, respectively. The bottom row presents the corresponding processed radiographs, demonstrating how variations in the $\varvec{\delta}$-map distribution directly modulate edge preservation, contrast amplification, and noise reduction. In Fig. 7(a), the yellow arrow indicates the internal substrate structure of the PCB. Because this region exhibits extremely low contrast, the linear, sigmoid, and tanh functions (Figs. 7(a), (b), and (d)) fail to distinguish these structural components from background noise, thereby limiting resolution enhancement within low-contrast areas. Conversely, while the gamma function (Fig. 7(c)) successfully preserves the low-contrast structure, it simultaneously falsely amplifies surrounding background noise as edges. Currently, the shape of the nonlinear mapping function must be manually configured. Because different imaging modalities, such as PCB X-ray, medical ultrasound, or industrial CT, possess distinct structural and statistical noise characteristics, manually tuning these mapping and spatial parameters is highly inefficient. To overcome this limitation while preserving the interpretability of our proposed framework, a hybrid approach is required. By employing a lightweight data-driven parameter optimizer, the model can autonomously adapt to the inherent statistical characteristics of a specific imaging domain. This would yield optimally tuned parameters without extensive computational overhead.

Nevertheless, there is still considerable scope for further structural optimization. Conventional Gaussian kernels are employed to suppress noise prior to the gradient map calculation in Eq. (1) and to isolate the high-frequency residual components in Eq. (5). Because these filtering stages are structurally independent, they can be integrated with or substituted by other noise reduction algorithms. Additionally, the framework evaluates local structural characteristics using a single-scale gradient magnitude. However, the actual structural components within PCB radiographic images exhibit

multiscale characteristics. Consequently, incorporating a Hessian-based ridge detection framework or a Laplacian-of-Gaussian (LoG) multiscale feature map is expected to significantly enhance the structural separation capability of the $\varvec{\delta}$-map.

5. Conclusion

This study presented a δ-map-based adaptive image processing technique that automatically modulates between localized sharpening and smoothing at the pixel level according to the structural salience of the image. By computing a spatially variant control map from the gradient magnitude of the input image and applying it to a residual-based architecture, the framework effectively mitigates the resolution-noise trade-off inherent to conventional global filters. Experimental evaluations conducted on PCB X-ray datasets demonstrated that the proposed method yields consistent performance improvements over conventional Gaussian, UM, bilateral, guided, and MUSICA methods in terms of structural sharpness, noise suppression, and perceptual naturalness. These improvements were rigorously validated not only through full-reference metrics (SSIM, PSNR, LPIPS) and no-reference metrics (BRISQUE, NIQE, PIQE) but also through frequency-domain performance evaluation metrics (MTF, NNPS, NEQ). Given its algorithmic simplicity, real-time efficiency, and analytical interpretability, the proposed framework can be practically utilized in radiological diagnostics and industrial NDT environments. Future work will focus on integrating multiscale structural analysis and Hessian-based ridge salience detection with the $\varvec{\delta}$-map framework to achieve advanced structural extraction and robust artifact suppression.

Declarations

6. Acknowledgement

This research was supported by National Measurement Standards Services and Technical Services for SME funded by Korea Research Institute of Standards and Science (KRISS-GP2026-0014-03).

7. Declaration of generative AI and AI-assisted technologies in the manuscript preparation process.

During the preparation of this work, the author utilized Gemini Pro (Google, Version May 2026) to refine academic English phrasing, translate technical descriptions, and organize the manuscript sections based on the experimental methodology. All scientific claims, mathematical derivations, and final text variants were reviewed, verified, and approved by the authors, who take full responsibility for the integrity of the content.

8. Data Availability

The datasets generated during and/or analysed during the current study are available from the corresponding author on reasonable request.

9. Competing Interests

The authors declare that they have no competing interests.

References

[1] Barrett, H. H., & Myers, K. J. (2013). *Foundations of image science*. John Wiley & Sons.

[2] Sado, A., & Hayward, J. P. (2026). Experimental Demonstration of 450kVp MesoFocus X-Ray Radiography for Rail Weld Inspection. *Journal of Nondestructive Evaluation*, *45*(2), 62. https://doi.org/10.1007/s10921-026-01352-8

[3] Chmieliński, Z., Klimaszewski, J., Kosiński, T., Kowalczyk, D., Matusiak, M., Rzadkiewicz, J., ... & Zakrzewski, T. (2025). Feasibility Study of Radiographic Rail Inspections Using a Compact X-ray Tube. *Journal of Nondestructive Evaluation*, *44*(2), 57. https://doi.org/10.1007/s10921-025-01193-x

[4] Cunningham, I. A., & Shaw, R. (1999). Signal-to-noise optimization of medical imaging systems. *Journal of the optical society of America A*, *16*(3), 621-632. https://doi.org/10.1364/JOSAA.16.000621

[5] Boncelet, C. (2009). Image noise models. In *The essential guide to image processing* (pp. 143-167). Academic Press. https://doi.org/10.1016/B978-0-12-374457-9.00007-X

[6] Mafi, M., Martin, H., Cabrerizo, M., Andrian, J., Barreto, A., & Adjouadi, M. (2019). A comprehensive survey on impulse and Gaussian denoising filters for digital images. *Signal Processing*, *157*, 236-260. https://doi.org/10.1016/j.sigpro.2018.12.006

[7] Burgess, A. E. (1999). The Rose model, revisited. *Journal of the Optical Society of America A*, *16*(3), 633-646. https://doi.org/10.1364/JOSAA.16.000633

[8] Cunningham, I. A. (2000). Applied linear-systems theory. *Handbook of medical imaging*, *1*, 79-159. https://doi.org/10.1117/3.832716.ch2

[9] Boone, J. M., & Seibert, J. A. (1997). An accurate method for computer-generating tungsten anode x-ray spectra from 30 to 140 kV. *Medical physics*, *24*(11), 1661-1670. https://doi.org/10.1118/1.597953

[10] Tomasi, C., & Manduchi, R. (1998, January). Bilateral filtering for gray and color images. In *Sixth international conference on computer vision (IEEE Cat. No. 98CH36271)* (pp. 839-846). IEEE. https://doi.org/10.1109/ICCV.1998.710815

[11] He, K., Sun, J., & Tang, X. (2013). "Guided image filtering." *IEEE Transactions on Pattern Analysis and Machine Intelligence*, 35(6), 1397–1409. https://doi.org/10.1109/TPAMI.2012.213

[12] Buades, A., Coll, B., & Morel, J. M. (2005, June). A non-local algorithm for image denoising. In *2005 IEEE computer society conference on computer vision and pattern recognition (CVPR'05)* (Vol. 2, pp. 60-65). Ieee. https://doi.org/10.1109/CVPR.2005.38

[13] Rudin, L. I., Osher, S., & Fatemi, E. (1992). Nonlinear total variation based noise removal algorithms. *Physica D: nonlinear phenomena*, *60*(1-4), 259-268. https://doi.org/10.1016/0167-2789(92)90242-F

[14] Perona, P., & Malik, J. (1990). Scale-space and edge detection using anisotropic diffusion. *IEEE Transactions on pattern analysis and machine intelligence*, *12*(7), 629-639. https://doi.org/10.1109/34.56205

[15] Kim, J., Oh, S., & Kim, H. K. (2023). Fourier analysis of multi-scale neural networks implemented for high-resolution X-ray radiography. *NDT & E International*, *139*, 102923. https://doi.org/10.1016/j.ndteint.2023.102923

[16] Wang, Z., Chen, J., & Hoi, S. C. (2020). Deep learning for image super-resolution: A survey. *IEEE transactions on pattern analysis and machine intelligence*, *43*(10), 3365-3387. https://doi.org/10.1109/TPAMI.2020.2982166

[17] Zhang, K., Ren, W., Luo, W., Lai, W. S., Stenger, B., Yang, M. H., & Li, H. (2022). Deep image deblurring: A survey. *International Journal of Computer Vision*, *130*(9), 2103-2130. https://doi.org/10.1007/s11263-022-01633-5

[18] Bellens, S., Guerrero, P., Vandewalle, P., & Dewulf, W. (2024). Machine learning in industrial X-ray computed tomography–a review. *CIRP Journal of Manufacturing Science and Technology*, *51*, 324-341. https://doi.org/10.1016/j.cirpj.2024.05.004

[19] Wang, Z., Bovik, A. C., Sheikh, H. R., & Simoncelli, E. P. (2004). "Image quality assessment: from error visibility to structural similarity." *IEEE transactions on image processing*, 13(4), 600-612. https://doi.org/10.1109/TIP.2003.819861

[20] Hore, A., & Ziou, D. (2010, August). "Image quality metrics: PSNR vs. SSIM." *In 2010 20th international conference on pattern recognition* (pp. 2366-2369). IEEE. https://doi.org/10.1109/ICPR.2010.579

[21] Zhang, R., Isola, P., Efros, A. A., Shechtman, E., & Wang, O. (2018). "The unreasonable effectiveness of deep features as a perceptual metric." *In Proceedings of the IEEE conference on computer vision and pattern recognition* (pp. 586-595). https://doi.org/10.1109/CVPR.2018.00068

[22] Mittal, A., Moorthy, A. K., & Bovik, A. C. (2012). "No-reference image quality assessment in the spatial domain." *IEEE Transactions on image processing*, 21(12), 4695-4708. https://doi.org/10.1109/TIP.2012.2214050

[23] Mittal, A., Soundararajan, R., & Bovik, A. C. (2012). "Making a completely blind image quality analyzer." *IEEE Signal processing letters*, 20(3), 209-212. https://doi.org/10.1109/LSP.2012.2227726

[24] Venkatanath, N., Praneeth, D., Bh, M. C., Channappayya, S. S., & Medasani, S. S. (2015, February). "Blind image quality evaluation using perception based features." *In 2015 Twenty First National Conference on Communications (NCC)* (pp. 1-6). IEEE. https://doi.org/10.1109/NCC.2015.7084843

[25] Dobbins III, J. T. (2000). Image quality metrics for digital systems. *Handbook of medical imaging*, *1*, 161-222. https://doi.org/10.1117/3.832716.ch3

[26] Canny, J. (1986). A computational approach to edge detection. *IEEE Transactions on pattern analysis and machine intelligence*, (6), 679-698. https://doi.org/10.1109/TPAMI.1986.4767851

[27] McIlhagga, W. (2011). The canny edge detector revisited. *International Journal of Computer Vision*, *91*(3), 251-261. https://doi.org/10.1007/s11263-010-0392-0

[28] Vincent, O. R., & Folorunso, O. (2009, June). A descriptive algorithm for sobel image edge detection. In *Proceedings of informing science & IT education conference (InSITE)* (Vol. 40, pp. 97-107). https://doi.org/10.28945/3351

[29] Petrou, M. M., & Petrou, C. (2010). *Image processing: the fundamentals*. John Wiley & Sons.

[30] Musa, P., Al Rafi, F., & Lamsani, M. (2018, October). A Review: Contrast-Limited Adaptive Histogram Equalization (CLAHE) methods to help the application of face recognition. In *2018 third international conference on informatics and computing (ICIC)* (pp. 1-6). IEEE. https://doi.org/10.1109/IAC.2018.8780492

[31] Polesel, A., Ramponi, G., & Mathews, V. J. (2000). Image enhancement via adaptive unsharp masking. *IEEE transactions on image processing*, *9*(3), 505-510. https://doi.org/10.1109/83.826787

[32] Burt, P. J., & Adelson, E. H. (1987). The Laplacian pyramid as a compact image code. In *Readings in computer vision* (pp. 671-679). https://doi.org/10.1016/B978-0-08-051581-6.50065-9

[33] Vuylsteke, P., & Schoeters, E. P. (1994, May). Multiscale image contrast amplification (MUSICA). In *Medical Imaging 1994: Image Processing* (Vol. 2167, pp. 551-560). SPIE. https://doi.org/10.1117/12.175090

[34] Kim, J., Yoo, S., Kim, J., & Kim, H. K. (2022). Towards subtraction angiography using a multi-layered X-ray detector. *Physica Medica*, *95*, 32-40. https://doi.org/10.1016/j.ejmp.2022.01.001

[35] Kim, H. K., Cho, M. K., Achterkirchen, T., & Lee, W. (2009). Radiation effects on the performance of CMOS photodiode array detectors and the role of gain-offset corrections. *IEEE Transactions on Nuclear Science*, *56*(3), 1179-1183. https://doi.org/10.1109/TNS.2009.2014232

[36] Park, C. J., Lee, H. K., Song, W. Y., Achterkirchen, T. G., & Kim, H. K. (2011). Defective pixel map creation based on wavelet analysis in digital radiography detectors. *Nuclear Instruments and Methods in Physics Research Section A: Accelerators, Spectrometers, Detectors and Associated Equipment*, *634*(1), 101-105. https://doi.org/10.1016/j.nima.2011.01.03

[37] Fujita, H., Tsai, D. Y., Itoh, T., Doi, K., Morishita, J., Ueda, K., & Ohtsuka, A. (1992). A simple method for determining the modulation transfer function in digital radiography. *IEEE Transactions on medical imaging*, *11*(1), 34-39. https://doi.org/10.1109/42.126908

[38] Obaton, A. F., Ewert, U., Roth, H., Wilbig, J., Brouczek, D., Schwentenwein, M., ... & Katic, M. (2025). Determination of the Image Quality in Computed Tomography and its Standardisation. *Journal of Nondestructive Evaluation*, *44*(4), 128. https://doi.org/10.1007/s10921-025-01266-x

[39] Janczynski, J., Tewes, A., Ulbricht, A., & Jaenisch, G. R. (2025). Evaluation Metrics for Comparison between Virtual and Industrial XCT. *Journal of Nondestructive Evaluation*, *44*(4), 120. https://doi.org/10.1007/s10921-025-01213-w

[40] *IEC 62220-1-3* (2008). Medical electrical equipment - Characteristics of digital X-ray imaging devices - Part 1-3: Determination of the detective quantum efficiency - Detectors used in dynamic imaging.
[41] Boone, J. M., & Seibert, J. A. (1994). An analytical edge spread function model for computer fitting and subsequent calculation of the LSF and MTF. *Medical physics*, *21*(10), 1541-1545. https://doi.org/10.1118/1.597264

[42] Samei, E., Flynn, M. J., & Reimann, D. A. (1998). A method for measuring the presampled MTF of digital radiographic systems using an edge test device. *Medical physics*, *25*(1), 102-113. https://doi.org/10.1118/1.598165

[43] Tapiovaara, M. J., & Wagner, R. (1985). SNR and DQE analysis of broad spectrum x-ray imaging. *Physics in Medicine & Biology*, *30*(6), 519-529. https://doi.org/10.1088/0031-9155/30/6/002

Figures

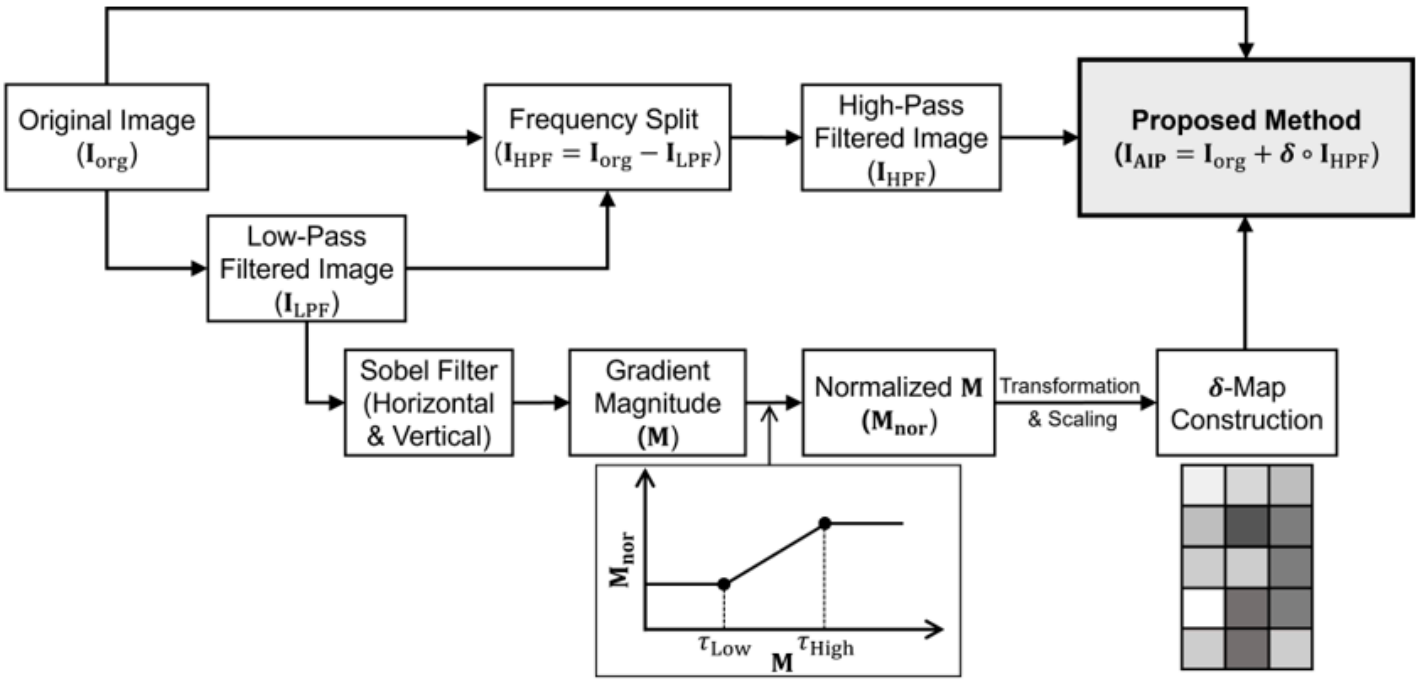


Figure 1

Flowchart of the proposed δ-map adaptive image processing (δ-AIP) algorithm.

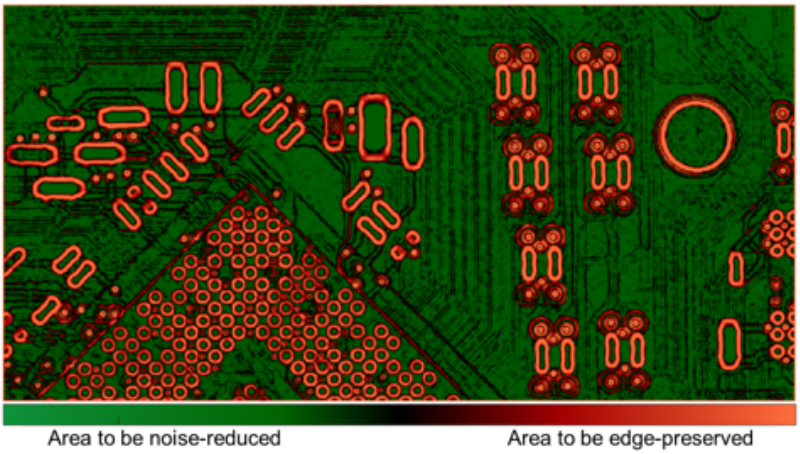


Figure 2

Visual representation of the δ-map identifying noise-sensitive and edge-critical regions in the PCB X-ray image. Green areas denote low-gradient, homogeneous regions targeted for noise reduction (suppressing texture amplification), whereas red-highlighted areas indicate high-gradient structural components requiring edge preservation.

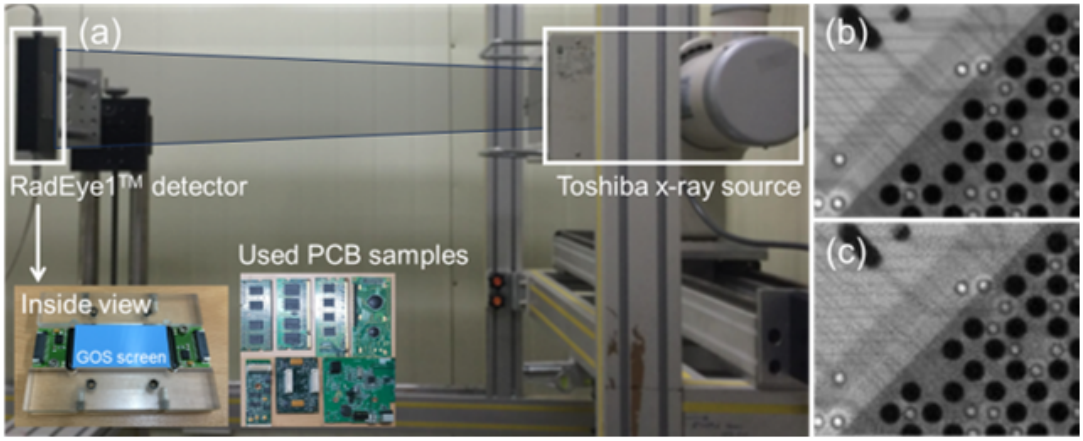


Figure 3

Experimental setup and acquired PCB dataset. (a) Configuration of the laboratory-scale X-ray imaging system comprising a tungsten X-ray tube and a RadEye1™ CMOS detector. (b) Clean reference PCB image after calibration procedures. (c) Synthetic noisy image generated by adding Gaussian noise to evaluate the noise suppression performance.

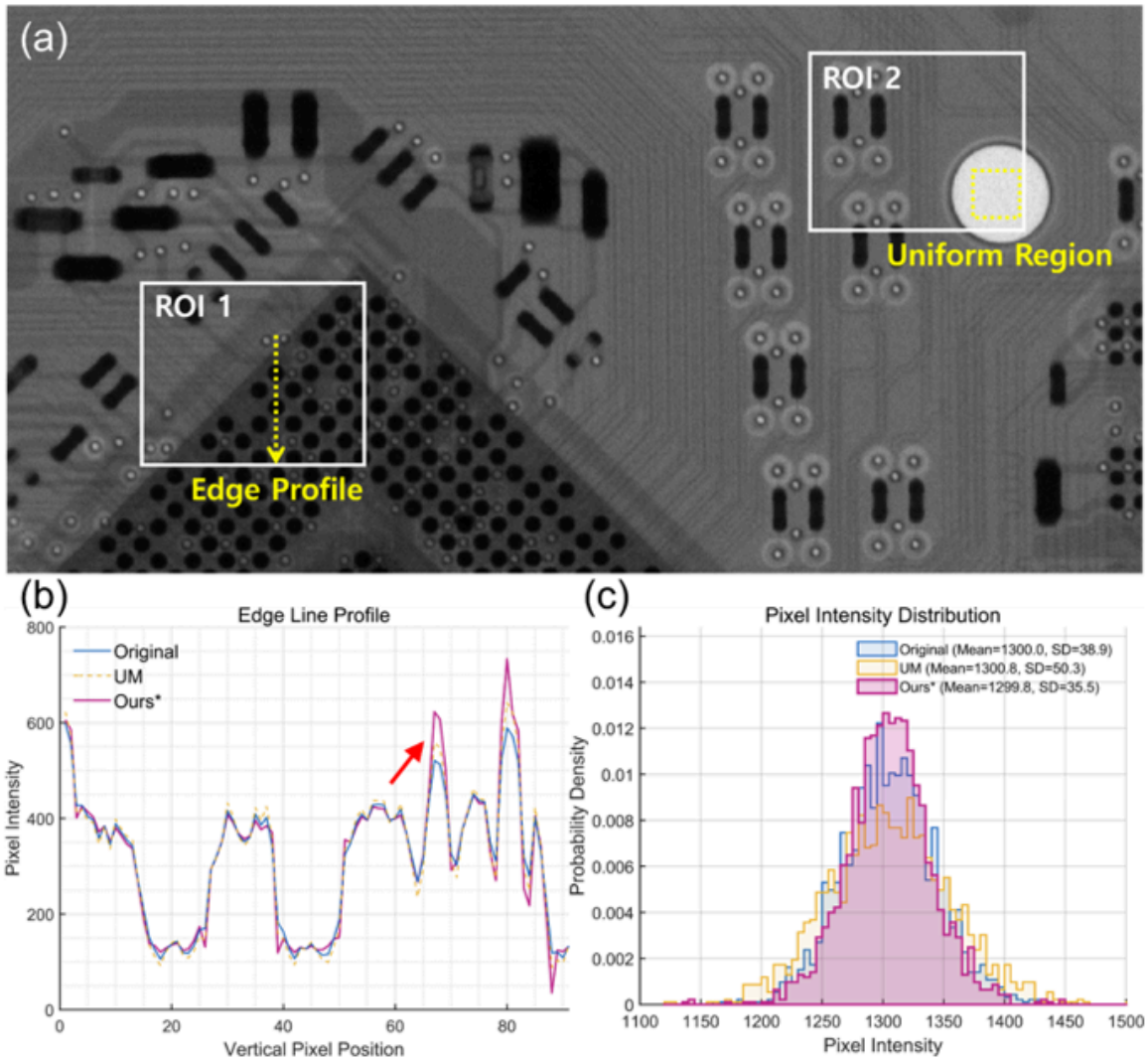


Figure 4

Evaluation of the proposed method on a PCB radiograph. (a) The original radiograph indicating the regions of interest (ROIs) for analysis: a vertical yellow dashed arrow represents edge profiling in ROI 1 and a yellow dashed box indicates uniform region in ROI 2. (b) The edge line profile extracted from ROI 1, demonstrating that the proposed method (Ours*) maintains sharp edge profiles comparable to UM, as highlighted by red arrow. (c) The pixel intensity distribution from the uniform region in ROI 2, confirming that the proposed method effectively suppresses noise (SD = 35.5) while preserving the mean signal intensity compared to the original and conventional UM methods.

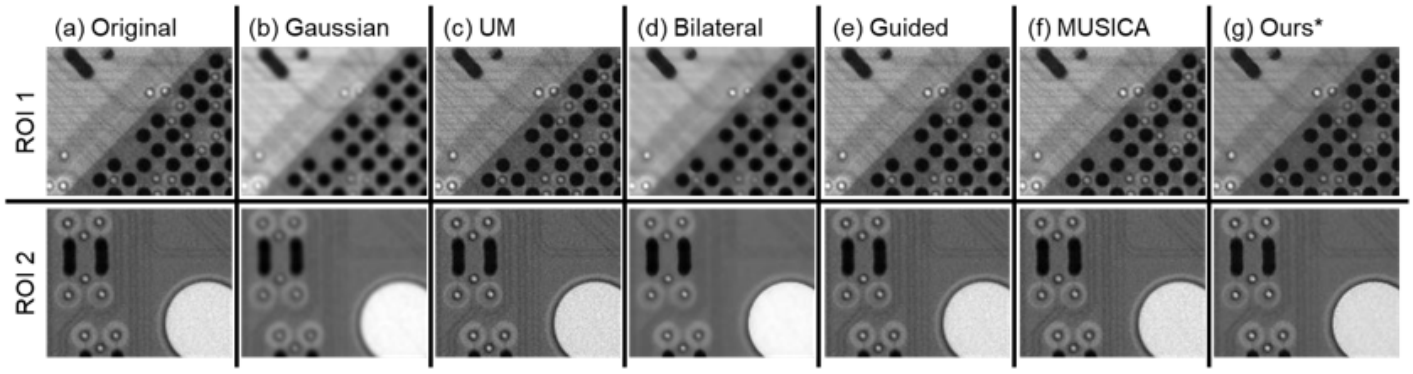


Figure 5

Qualitative comparison of enhanced PCB X-ray images (ROI 1 and 2 in Fig. 4 (a)) obtained using different algorithms: (a) original, (b) Gaussian filter, (c) unsharp masking (UM), (d) bilateral filter, (e) guided filter, (f) MUSICA, and (g) the proposed method.

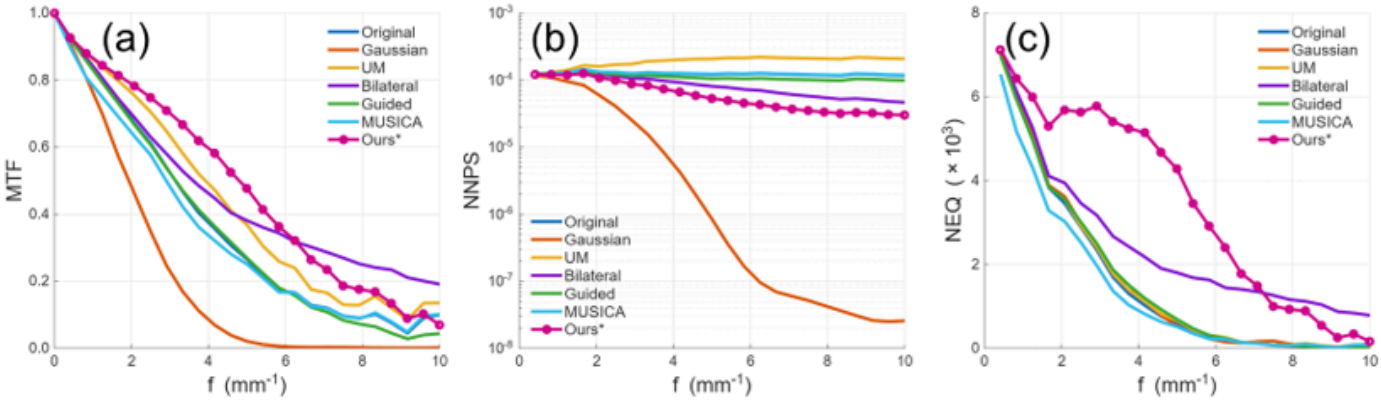


Figure 6

Frequency-domain performance evaluation of the proposed δ-map adaptive image processing method. (a) MTF, (b) Normalized NPS, (c) NEQ.

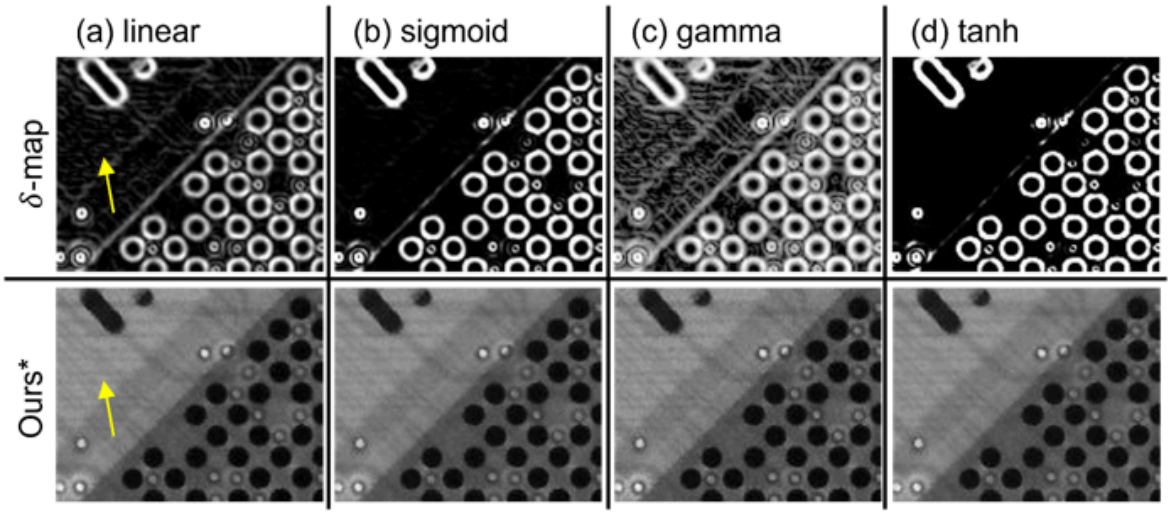


Figure 7

Comparison of δ-maps generated by different nonlinear mapping functions and the corresponding enhanced radiographs: (a) linear, (b) sigmoid, (c) gamma, (d) tanh. The yellow arrow indicates the internal substrate structure in the PCB.